

Structure of central and southern Mexico from velocity and attenuation tomography

Ting Chen¹ and Robert W. Clayton¹

Received 13 February 2012; revised 18 June 2012; accepted 20 July 2012; published 5 September 2012.

[1] The 3D V_p , V_p/V_s , P- and S-wave attenuation structure of the Cocos subduction zone in Mexico is imaged using earthquakes recorded by two temporary seismic arrays and local stations. Direct P wave arrivals on vertical components and direct S wave arrivals on transverse components from local earthquakes are used for velocity imaging. Relative delay times for P and PKP phases from teleseismic events are also used to obtain a deeper velocity structure beneath the southern seismic array. Using a spectral-decay method, we calculate a path attenuation operator t^* for each P and S waveform from local events, and then invert for 3D spatial variations in attenuation (Q_p^{-1} and Q_s^{-1}). Inversion results reveal a low-attenuation and high-velocity Cocos slab. The slab dip angle increases from almost flat in central Mexico near Mexico City to about 30° in southern Mexico near the Isthmus of Tehuantepec. High attenuation and low velocity in the crust beneath the Trans-Mexico Volcanic Belt correlate with low resistivity, and are probably related to dehydration of the slab and melting processes. The most pronounced high-attenuation, low- V_p and high- V_p/V_s anomaly is found in the crust beneath the Veracruz Basin. A high-velocity structure dipping into the mantle from the side of Gulf of Mexico coincides with a discontinuity from a receiver functions study, and provides an evidence for the collision between the Yucatán Block and Mexico in the Miocene.

Citation: Chen, T., and R. W. Clayton (2012), Structure of central and southern Mexico from velocity and attenuation tomography, *J. Geophys. Res.*, 117, B09302, doi:10.1029/2012JB009233.

1. Introduction

[2] In the Mexican subduction zone, the Rivera and Cocos Plates subduct beneath the North American Plate along the Middle America Trench (Figure 1). Although the subduction rate and plate age of the subducting plates both monotonically increase toward the southeast, the seismicity studies [Pardo and Suárez, 1995] suggest that the slab transitions from normal subduction in the north (Jalisco, Michoacán) to shallow subduction in the central segment (Guerrero), and then back to normal subduction in the south (Oaxaca). However, since the seismicity in central Mexico is sparse, the detailed structure of the slab and how the slab transitions from shallow to normal subduction is not well known.

[3] The volcano distribution in this subduction zone also shows anomalous features. Volcanoes progressively shift from northern to central Mexico, and are about 300 km away from the trench near Mexico City, forming the Trans-Mexican Volcanic Belt (TMVB) with about a 16° angle to the trench. In

southern Mexico, the continuous volcanic arc is missing where the Cocos slab is about 100 km deep, which is the typical depth for melt generation in subduction zones [Wada and Wang, 2009]. Instead, the isolated Los Tuxtlas Volcanic Field (LTVF) is found near the Gulf of Mexico coast, which is about 150–200 km above the Cocos slab based on the extrapolation of seismicity [Pardo and Suárez, 1995]. The TMVB is generally considered to be related to the subduction of the oceanic plate, with the volcano distribution following the geometry of the slab. The mechanisms of the origin of the LTVF, however, are unclear [e.g., Nelson et al., 1995; Ferrari et al., 2005; Verma, 2006].

[4] A knowledge of the velocity structure in Mexico is important to an understanding of the tectonic evolution of the subduction system. Studies on the velocity of the crust and upper mantle in this region have been done using active sources and earthquakes [e.g., Meyer et al., 1961; Valdes et al., 1986; Gomberg and Masters, 1988; Gomberg et al., 1988; Campillo et al., 1996; Shapiro et al., 1997]. Most of these studies concentrate on small areas or only develop 1D models. A detailed 3D velocity model is needed to better understand the tectonic features.

[5] Large coastal earthquakes pose a great threat to heavily populated Mexico City. Understanding what level of ground motions to expect in Mexico City from an earthquake is essential to effective hazard mitigation. Many attenuation studies have thus been conducted [e.g., Castro et al., 1990;

¹Seismological Laboratory, California Institute of Technology, Pasadena, California, USA.

Corresponding author: T. Chen, Seismological Laboratory, California Institute of Technology, MC 252-21, Pasadena, CA 91125, USA. (tchen@gps.caltech.edu)

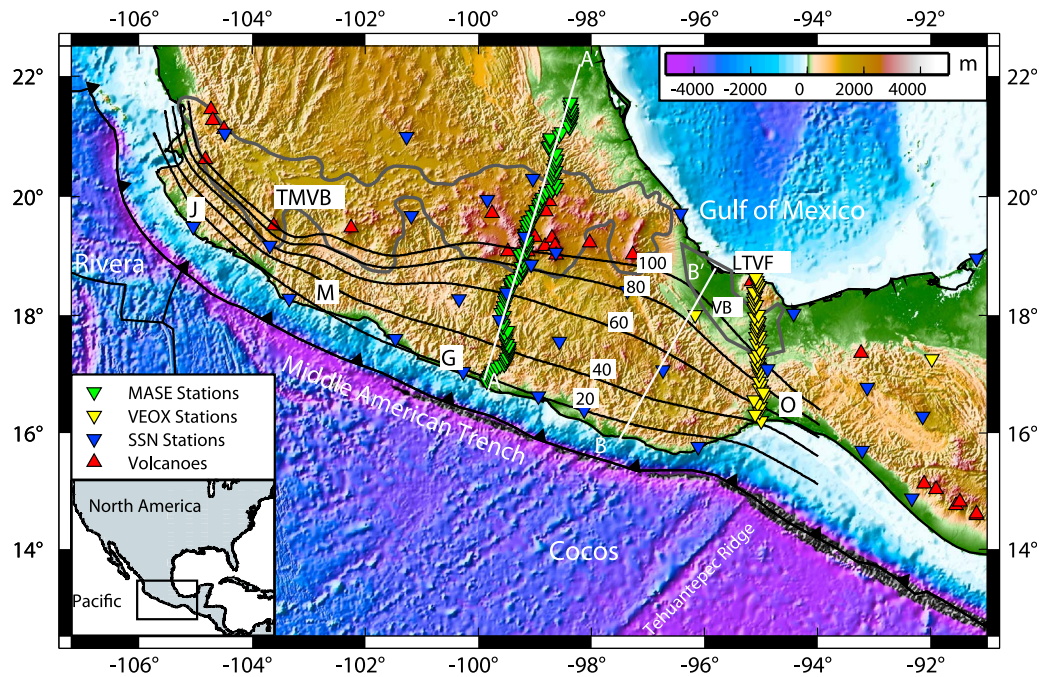


Figure 1. Map of the study region. Stations are marked by inverted triangles, and volcanoes are marked by red upright triangles. The Trans-Mexican Volcanic Belt (TMVB) and Veracruz Basin (VB) are outlined in light gray. White lines AA' and BB' are two MT surveys in *Jödicke et al.* [2006]. LTVF denotes the Los Tuxtlas Volcanic Field. J (Jalisco), M (Michoacán), G (Guerrero), and O (Oaxaca) indicate four segments in this region. Slab iso-depth contours from *Pardo and Suárez* [1995] are shown by black lines.

Ordaz and Singh, 1992; *Yamamoto et al.*, 1997; *Garcia et al.*, 2004; *Singh et al.*, 2006, 2007], but due to limited data, most of the studies are restricted to certain regions, and the results are path-averaged values. Attenuation tomography has also been done in this region [*Ottmöller et al.*, 2002], but it is of low spatial resolution, and only for Lg waves. More detailed attenuation tomography resolving both the crust and the upper mantle is necessary to understand the subduction process. Attenuation complements the velocity studies, and helps to constrain the origin of anomalies.

[6] Recently, a seismic array has been deployed in the Guerrero segment from Acapulco to the Gulf of Mexico. Receiver function studies [*Pérez-Campos et al.*, 2008; *Kim et al.*, 2010] along this array confirm the shallow subduction in central Mexico, and show that the Cocos slab is sub-horizontal for about 250 km from the trench. Teleseismic velocity study images the deeper structure of the Cocos slab, and shows that the slab descends steeply (75°) into the mantle to a depth of 500 km beneath the TMVB [*Husker and Davis*, 2009]. Surface waves reveal low velocity in the back arc, particularly in the lower crust beneath the TMVB [*Iglesias et al.*, 2010]. The 2D attenuation images show relatively high attenuation in the mantle wedge and the lower crust beneath the TMVB [*Chen and Clayton*, 2009]. These studies along the same line provide a detailed 2D image of the subduction system from the coast to the back arc.

[7] In this study, we seek to extend this image by constructing a 3D image of the subduction system in central and

southern Mexico using a second array to the southeast and the permanent local stations.

2. Data

[8] From 2005 to 2007, the Middle American Subduction Experiment (MASE) was conducted in central Mexico with a seismic line running perpendicular to the trench in the Guerrero region (Figure 1). A total of 100 three-component broadband sensors were spaced about 5 km apart. From 2007 to 2009, 47 seismometers were deployed in southern Mexico crossing the states of Veracruz and Oaxaca (VEOX). These two experiments, together with 46 stations of the National Seismological Service of Mexico (SSN), provide excellent data for detailed 3D velocity and attenuation imaging.

[9] In this study, we analyzed 894 local events with local magnitude between 3.5 and 5. Most of the events are deeper than 50 km. Crustal events are included only if the distance is less than 150 km to avoid the contamination of direct arrivals by other phases. The events are located by SSN using a 1D local velocity model (V. H. E. Castro and A. Iglesias, personal communication, 2012). The accuracy of the SSN catalogue is confirmed by a relocation study [*Alberto*, 2010]. We also used 200 teleseismic events recorded by the VEOX array to perform a teleseismic velocity study (Figure 2).

[10] For local events, arrival times are picked on the vertical component for the direct P wave and transverse component for the direct S wave. The algorithm based on the STA/LTA ratio is adopted to automate the picking process. The picked arrival

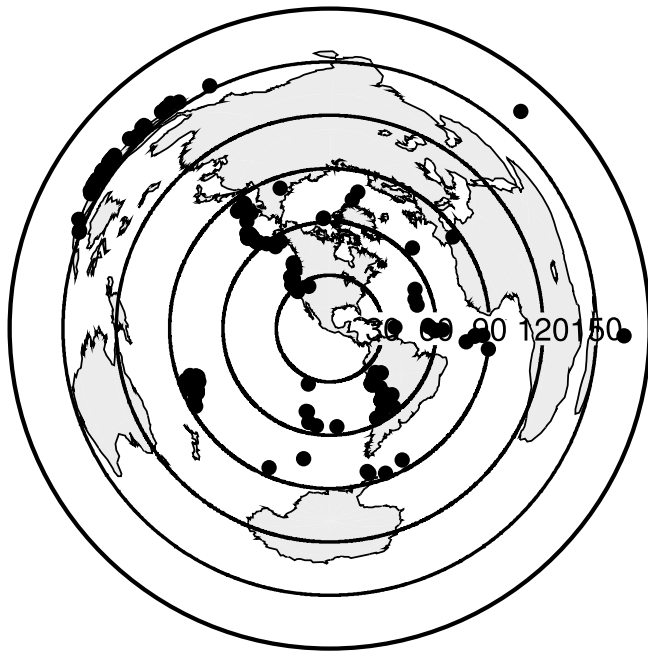


Figure 2. Distribution of events used for teleseismic study.

times are then manually checked. For teleseismic events, the relative delay times are determined by the cross correlation of each trace to a reference trace after bandpass filtering between 0.2 and 0.8 Hz. For distances between 30° and 90° , the P phase is used, and for the distances larger than 155° , the PKP_{df} phase is used.

3. Methods

3.1. Determining Attenuation Operator

[11] The whole path attenuation can be described by the attenuation operator $t^* = \tau/Q$, where τ is the travel time, and Q is the average quality factor along the path. The amplitude of the velocity spectrum of a body wave from event j , and recorded at station i , can be written as [Anderson and Hough, 1984]

$$A_{ij}(f) = CS_j(f)I_i(f)\exp(-\pi f t_{ij}^*), \quad (1)$$

where $I(f)$ is the instrument response, C is the frequency-independent amplitude term related to geometric spreading, radiation pattern, and other static effects. The exponential term represents the attenuation effect. Assuming a Brune-type source [Brune, 1970], the source term $S(f)$ can be expressed as

$$S_j(f) = \frac{f M_{0j}}{1 + (f/f_c)^2}, \quad (2)$$

where M_{0j} is the seismic moment, and f_c is the corner frequency. After removing instrument response, the spectral amplitude has the following form:

$$A_{ij}(f) = \frac{C'f}{1 + (f/f_c)^2} \exp(-\pi f t_{ij}^*), \quad (3)$$

with C' being a combined constant.

[12] We adopt the iterative approach of Eberhart-Phillips and Chadwick [2002] by first determining a common corner frequency f_c for each event using all the records from the event, and then obtaining frequency-independent t_{ij}^* and C' for each seismogram spectrum. We use the vertical component for the analysis of the P wave and transverse component for the analysis of the S wave. A 2.56 s time window starting from the onset of the arrival is used to calculate the signal spectrum, and a 2.56 s time window before the signal is used to calculate the noise spectrum. To ensure the high quality of t^* values used for the inversion, we apply the following selection criteria. For P waves, the signal-to-noise spectral ratio has to be larger than 2 over a 10 Hz frequency band from 2 to 40 Hz. For S waves, we lower the signal-to-noise ratio threshold to 1.5. For each event, there should be at least five t^* values. Unrealistic t^* values that correspond to Q larger than 3000 are also excluded. Examples of waveforms and spectral fits are shown in Figure 3.

3.2. Tomographic Inversion

[13] Arrival times for local P and S waves are inverted for 3D V_p and V_p/V_s structure using the package SIMUL2000 [Thurber, 1993; Eberhart-Phillips, 1993; Thurber and Eberhart-Phillips, 1999]. A total of 31,221 P picks from 894 local events and 18,710 S picks from 841 local events are used. We parameterize the model by 3D grid with interval spacing of 150 km along the trench, 20 km perpendicular to the trench, and 20 km in the depth direction (Figure 4). The initial model has P-wave velocities similar to the IASP91 model [Kennett and Engdahl, 1991], but with the Moho depth at 40 km based on receiver function studies in this region [Kim et al., 2010, 2011]. The initial V_p/V_s ratio is uniform, and has the value of 1.73. Ray tracing is done in two steps: the approximate ray tracing (ART), which selects the fastest smooth curve connecting the source and receiver, and the pseudobending, which further perturbs the ART ray to the true path ray [Um and Thurber, 1987]. This ray tracing procedure has been shown to be effective and accurate for 3D velocity models, especially when modified to improve the performance for long raypaths [Schurr et al., 2006]. Earthquakes are relocated during the velocity inversion. The solution is the result of an iterative, damped least squares inversion. The damping parameter is chosen based on the trade-off curve of data variance and model variance [Eberhart-Phillips, 1986].

[14] The attenuation parameters t_p^* and t_s^* are used to invert for 3D P-wave and S-wave attenuation structure in a manner similar to the inversion for velocity. A total of 15,699 t_p^* from 718 local events and 9968 t_s^* from 661 local events are used. Travel times are computed with rays traced in the 3D velocity model obtained in this study. The same grid as with the velocity inversion is used. The initial attenuation model has a constant Q of 800, to minimize the residuals of most t^* . We solve $1/Q$ for each grid node in an iterative procedure.

[15] We found that the noise levels on teleseismic records limit their usefulness in determining local attenuation structure. A 2D teleseismic velocity structure has already been obtained along the MASE array [Husker and Davis, 2009], and the local SSN stations are sparse between the MASE and VEOX arrays, so in this work we only invert for a 2D velocity structure along the VEOX array with the teleseismic study. Relative delay times for P and PKP_{df} phases are used

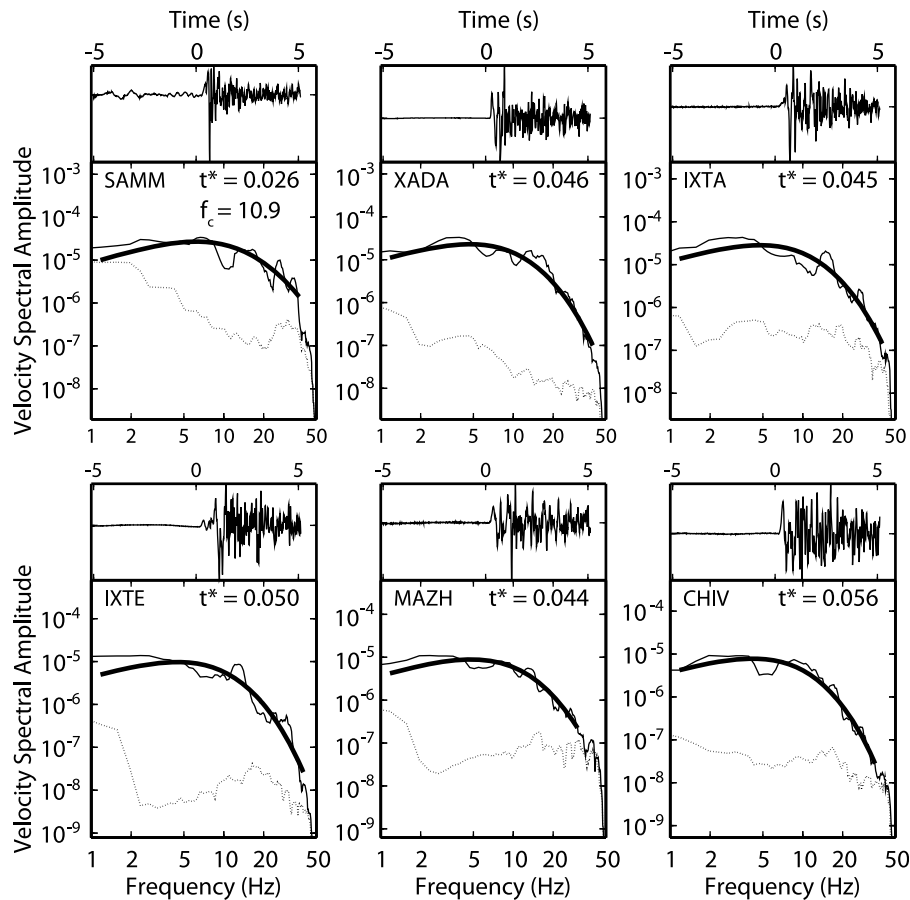


Figure 3. Examples of waveforms and t^* fits for one earthquake. For each station, the signal (solid line) and noise (dotted line) spectra are shown below the velocity waveform. The plotted velocity waveform is normalized by its peak amplitude. The fit to the spectrum is shown as a thick line over the range with adequate signal-to-noise ratio. A common corner frequency f_c for the event and different t^* for each record are estimated.

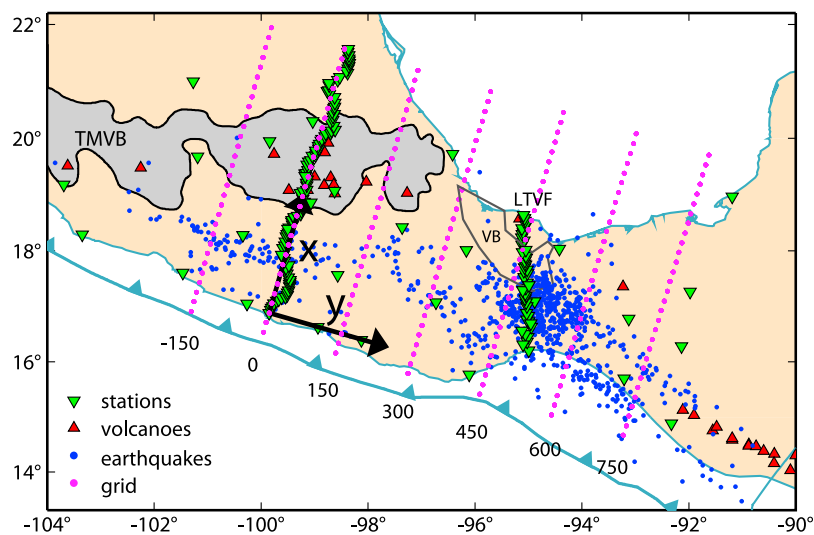


Figure 4. Grid, earthquakes, and stations used for velocity and attenuation inversion. The grid is spaced 150 km along the trench (y-axis), 20 km perpendicular to the trench (x-axis), and 20 km in the depth direction. Numbers denote the y coordinates of the grid in kilometer. TMVB: Trans-Mexican Volcanic Belt; VB: Veracruz Basin; LTVF: Los Tuxtles Volcanic Field.

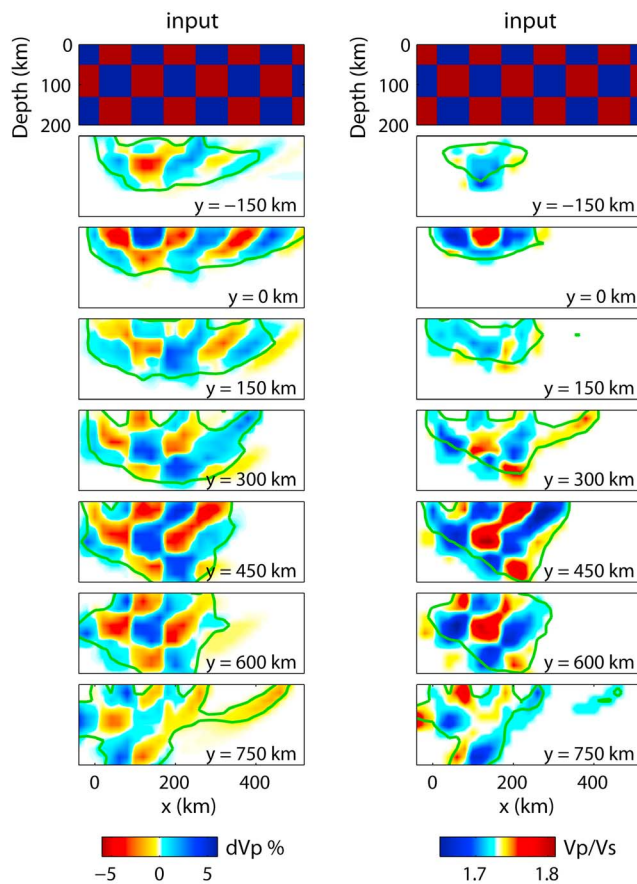


Figure 5. Checkerboard test for 3D P-velocity perturbation (left panel) and V_p/V_s (right panel) inversion. The top panels show the input models for slices at $y = -150$, 0 , and 150 km. The input models for slices at $y = 300$, 450 , 600 , and 750 km have opposite values of that shown in the top panels. The following panels are the recovered results for different slices along the x-axis. Green lines indicate the contour of the derivative weighted sum of 1000, and reasonably approximate the well-resolved region.

to invert for the teleseismic P-wave velocity perturbation in a manner similar to the inversion for local velocity.

4. Resolution

[16] We perform checkerboard tests to evaluate the resolution of the tomographic inversion. The input model consists of blocks of dimensions 80 km (x) \times 600 km (y) \times 80 km (z) with alternating positive and negative anomalies (Figures 5 and 6). Synthetic arrival times or attenuation operators are computed based on the input model, and then inverted in the same manner as the real data. Noise comparable to the residual level of the real data is added to the synthetic data.

[17] For V_p and Q_p , the crust is well resolved along the MASE ($y = 0$ km) and VEOX ($y = 450$ km) lines. The anomalies in the mantle near the VEOX line are also well recovered. The mantle near the MASE line is not resolved due to the absence of intermediate earthquakes in central Mexico. V_p/V_s and Q_s generally have relatively lower resolution than V_p and Q_p , especially in the arc and back arc near

the MASE line ($y = 0$ km). The streaks in the recovered models are related to dominant ray directions.

[18] The quality of solution can also be evaluated using the derivative weighted sum (DWS). The DWS measures the ray density in the neighborhood of each node. Tests have shown that DWS tracks well with diagonal elements of the resolution matrix, and high DWS values correspond to high resolution and low smearing [e.g., *Hauksson, 2000; Rietbrock, 2001*]. In Figures 5 and 6, the contours of DWS values of 1000 coincide with well recovered regions from checkerboard tests. The contours of DWS of 1000 also roughly correspond to the diagonal elements of the resolution matrix of 0.1. For the following plots of tomographic results, we use a DWS contour of 1000 to indicate the well resolved regions.

5. Results

5.1. Local Velocity and Attenuation

[19] P-wave velocity results show considerable variation across the studied region (Figure 7). High- V_p structure is

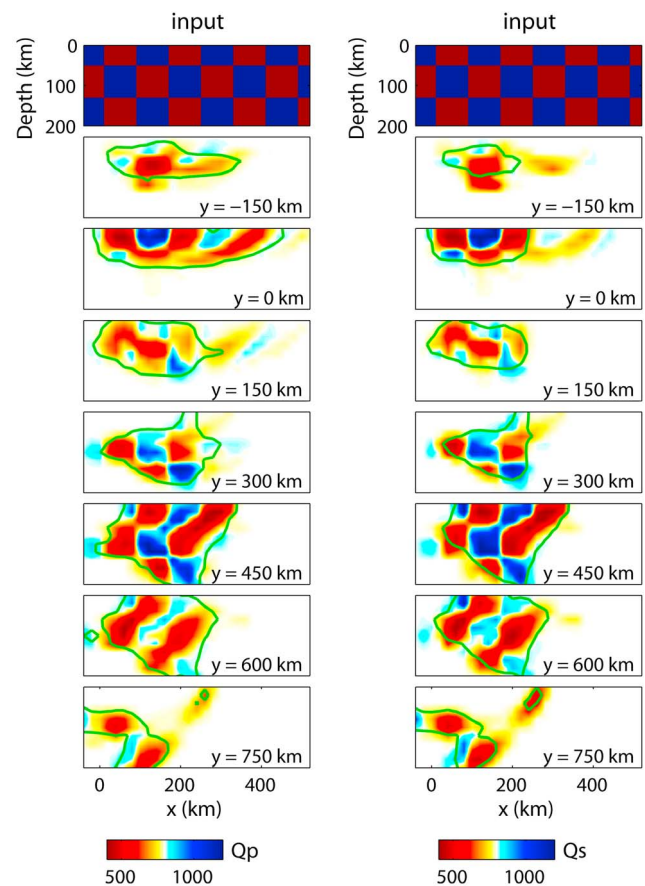


Figure 6. Checkerboard test for P-wave attenuation (left panel) and S-wave attenuation (right panel) inversion. The top panels show the input models for slices at $y = -150$, 0 , and 150 km. The input models for slices at $y = 300$, 450 , 600 , and 750 km have opposite values of that shown in the top panels. The following panels are the recovered results for different slices along the x-axis. Green lines indicate the contour of the derivative weighted sum of 1000, and reasonably approximate the well-resolved region.

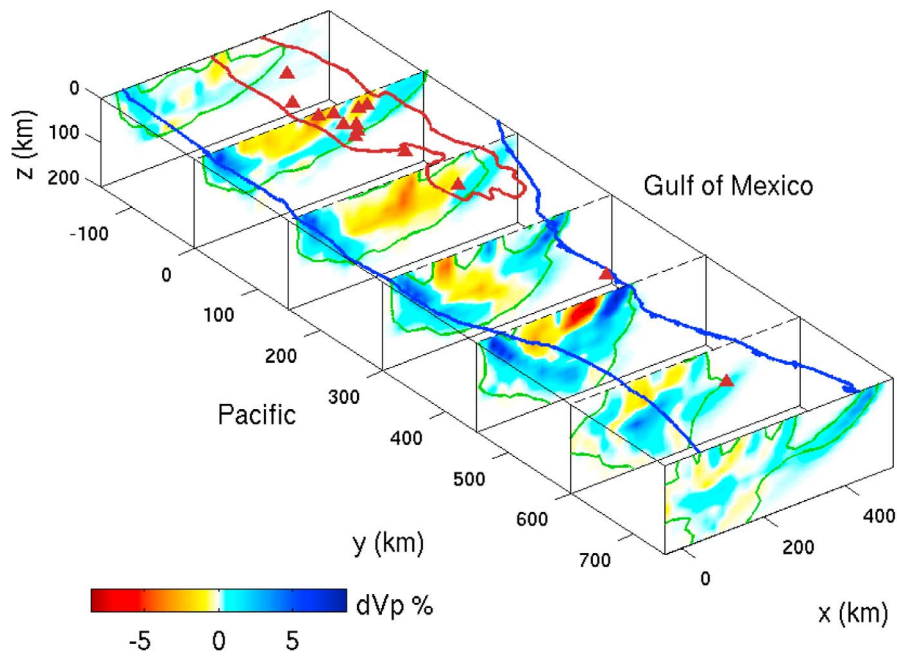


Figure 7. P-wave velocity perturbation results. Volcanoes are marked by red triangles. The TMVB and the coast are shown by red and blue lines respectively. Green lines are contours of the derivative weighted sum of 1000, and indicate the area with good resolution.

imaged dipping northeast from the Pacific coast. Another prominent high- V_p structure is near the Gulf of Mexico coast on the VEOX line ($y = 450$ km), which is beneath the LTVF. Relatively low V_p values are observed in some part of the crust and the mantle wedge. The lowest-velocity anomaly lies in the crust at about $x = 220$ km near the VEOX line ($y = 450$ km), which is beneath the Veracruz Basin (VB). The lowest V_p/V_s is found dipping southwest from the Gulf

of Mexico at $y = 450$ km, and the highest V_p/V_s is in the crust beneath the Veracruz Basin (Figure 8).

[20] P-wave attenuation results reveal a prominent low-attenuation ($Q \approx 1000$ – 2000) structure dipping northeast from the Pacific coast (Figure 9). The dip angle of this low-attenuation structure increases from about 0° in central Mexico ($y = 150$ km) to about 30° near the Isthmus of Tehuantepec ($y = 450$ km). The dip angle appears to be even

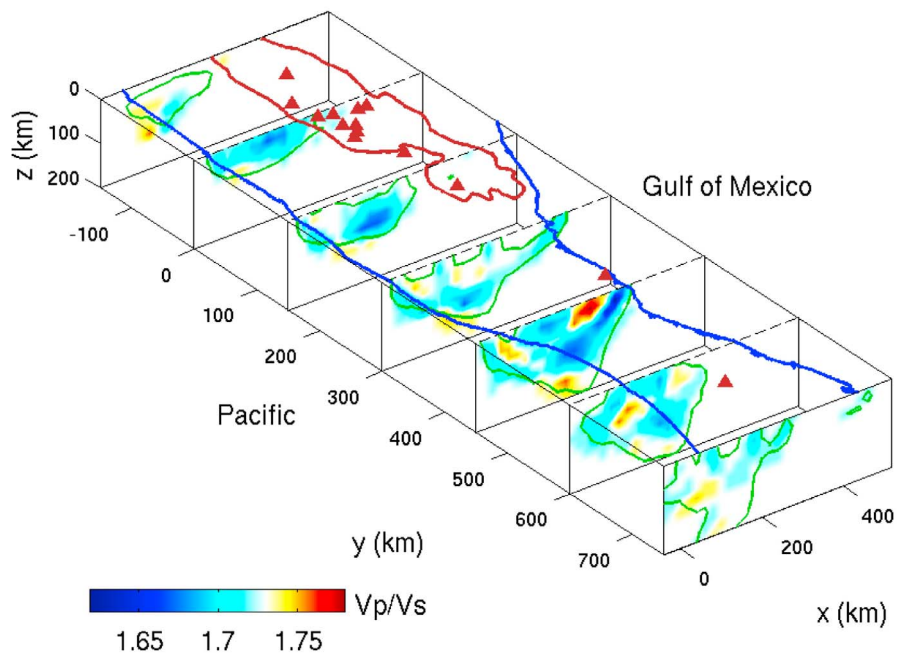


Figure 8. The V_p/V_s results. Symbols are the same as in Figure 7.

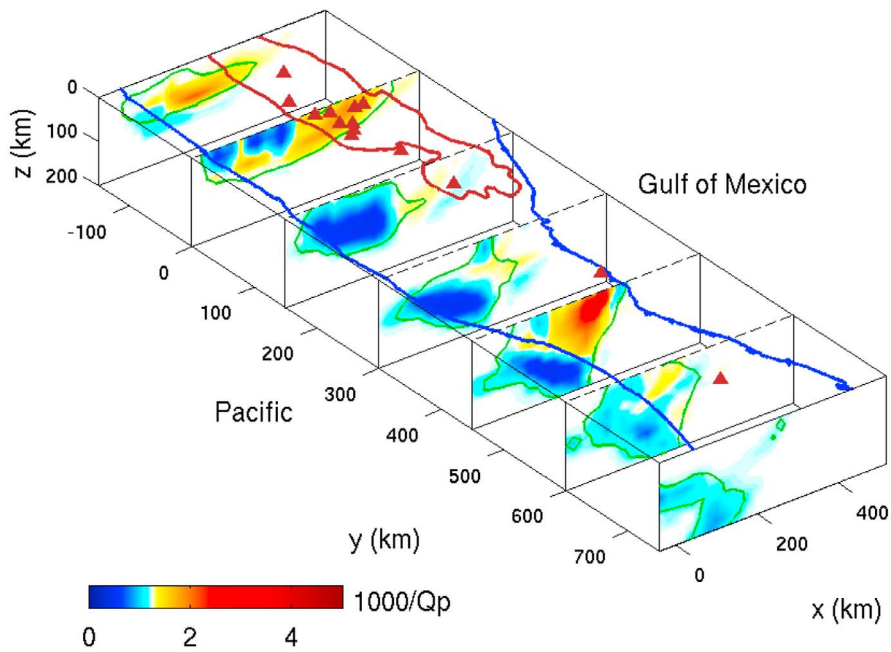


Figure 9. P-wave attenuation results. Symbols are the same as in Figure 7.

larger further to the south, but the resolution is limited. Low attenuation is also observed beneath the LTVF. The highest attenuation is imaged beneath the Veracruz Basin. A relatively high-attenuation anomaly is also found in the crust beneath the TMVB. S-wave attenuation results show similar features as the P-wave attenuation, but with stronger anomalies (Figure 10). The low- Q_p anomaly in the crust beneath the TMVB does not appear in S-wave attenuation results due to the lack of resolution.

[21] Resolution tests show that the slab could be well recovered along $y = 450$ km, with a little smearing into the crust (Figure 11). The anomaly in the upper crust could also be recovered, but with some smearing into the lower crust.

5.2. Teleseismic Velocity

[22] The teleseismic image along the VEOX array shows two dipping high-velocity structures (Figure 12). One is dipping northward from the Pacific, and the other unexpected one is dipping southward from the Gulf of Mexico.

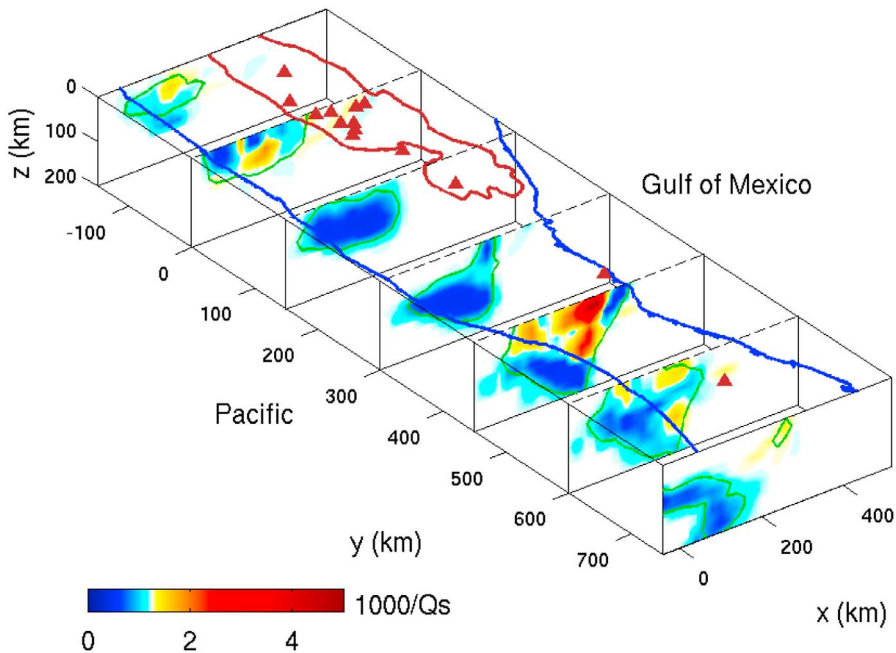


Figure 10. S-wave attenuation results. Symbols are the same as in Figure 7.

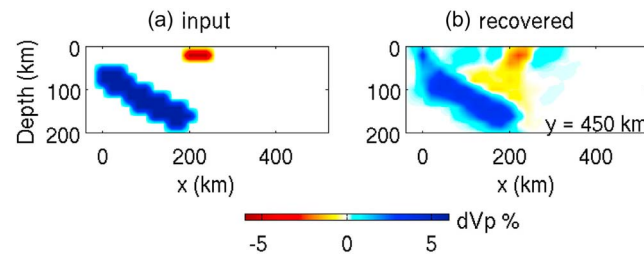


Figure 11. Synthetic recovery test. (a) The input model. (b) The recovered model along $y = 450$ km. Noise of normal distribution and amplitude comparable to the residual of real data is added to the synthetic data.

The high-velocity structure dipping from the Pacific follows the earthquakes with a little larger dip angle. The high-velocity structure dipping from the Gulf of Mexico correlates with the discontinuity found by the receiver function study [Kim *et al.*, 2011]. The stronger velocity anomaly also correlates with stronger receiver function signals. The dip angle of the unexpected high-velocity structure is larger than the dip angle of the discontinuity shown by the receiver functions, but with the empirical correction discussed in Appendix A, coincides with it. The high-velocity structure dipping from the Pacific is truncated by the high-velocity structure dipping from the Gulf of Mexico at the depth of about 150 km, and the truncation happens where the relocated events show a kink [Alberto, 2010]. In the crust, low velocity is found beneath the Veracruz Basin, and high velocity is located beneath the forearc and the LTVF.

[23] Resolution tests show that velocity anomalies dipping from either side can be resolved with a little smearing into the crust and the deeper mantle (Figures 13f and 13g). The recovered dip angle, however, differs slightly from the input. The bias in the inverted dip angle is not due to the specific data coverage in this study, but generally due to the limited range of incidence angles for teleseismic study. This bias becomes larger for shallower dipping structure (Appendix A). The high-velocity structure dipping from the Gulf of Mexico is not just a smearing effect of the crustal anomalies to depth (Figure 13h) or the smearing of localized anomalies (Figure 13i). The crustal variations in velocity can be resolved with our station spacing (Figure 13j).

6. Discussion

[24] The 3D velocity structure correlates well with the attenuation structure. The velocity and attenuation results for the two slices best resolved are compared in Figure 14 ($y = 0$ km, along the MASE array) and Figure 15 ($y = 450$ km, near the VEOX array). As with other studies in subduction zones [e.g., Tsumura *et al.*, 2000; Schurr *et al.*, 2003; Stachnik *et al.*, 2004; Rychert *et al.*, 2008], our inversion results show that the slab is characterized by low attenuation and high velocity. The slab is also generally associated with low V_p/V_s . It is noteworthy that the slab seems to be even more evident in attenuation than in velocity, which was also observed by Eberhart-Phillips *et al.* [2008]. The variation in the geometry of the Cocos slab is clearly imaged along the trench. The dip angle increases from about 0° in central Mexico near Mexico City to about 30° in southern Mexico near the Isthmus of Tehuantepec. Earthquakes are located within the high-velocity and low-attenuation slab. The cause

of flat subduction in central Mexico is not well understood [Skinner and Clayton, 2011], and this study does not indicate a mechanism for the flattening.

[25] High-attenuation and low-velocity anomalies are found in the crust. One such anomaly is in the crust beneath the TMVB near Mexico City (Figure 14). This structure has also been shown in surface waves [Iglesias *et al.*, 2010] and imaged in a 2D attenuation study in this region [Chen and Clayton, 2009]. The relatively higher value of attenuation found in Chen and Clayton [2009] compared to in this study is due to the different inversion schemes. In particular, this study inverts for the results using an iterative approach starting with an initial model where unrealistic values are rejected, while Chen and Clayton [2009] uses a simple one-step damped least squares inversion without any constraints

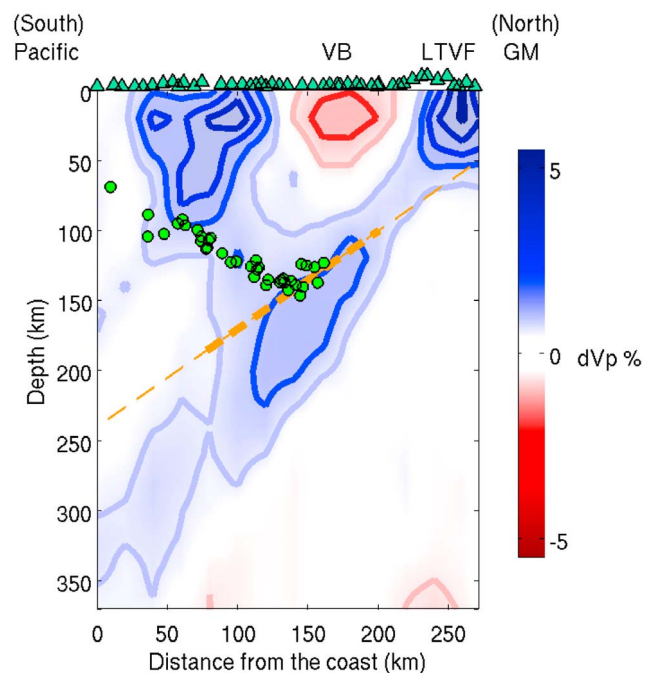


Figure 12. Teleseismic P-wave velocity perturbation inversion results along the VEOX array. Green dots denote the relocated events in this area [Alberto, 2010]. Dashed line shows the discontinuity found by the receiver function study [Kim *et al.*, 2011]; the most prominent part of the receiver function signals is highlighted by the thicker line. The green triangles are the VEOX stations. VB: Veracruz Basin; LTVF: Los Tuxtlas Volcanic Field; GM: Gulf of Mexico.

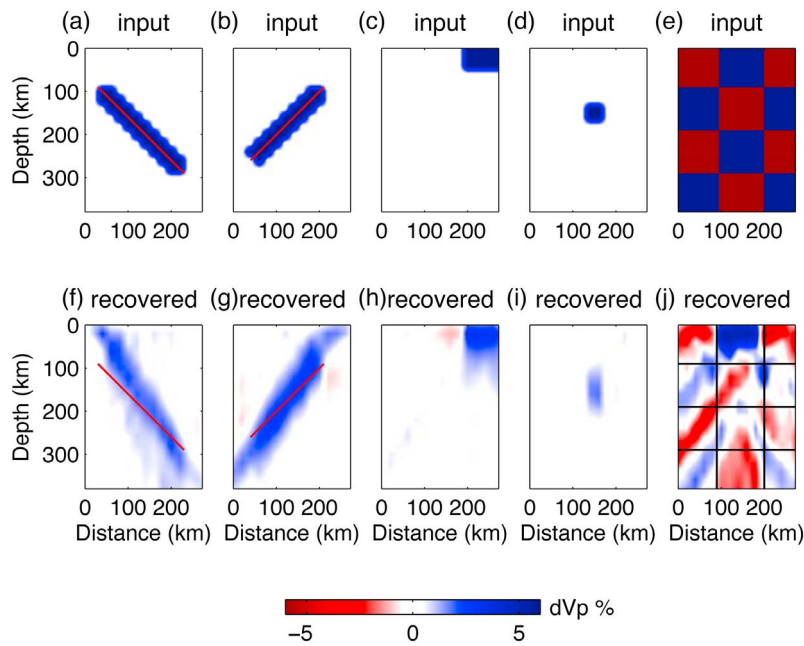


Figure 13. Resolution tests for the teleseismic P-wave velocity perturbation inversion. (a–e) The input models, (f–j) the recovered results. The noise added to the synthetic data is Gaussian and its amplitude is comparable to the residual of the real data. The x-axis is the distance from the coast along the VEOX array. The red lines in Figures 13f and 13g are for reference, and they are the same as in Figures 13a and Figures 13b respectively.

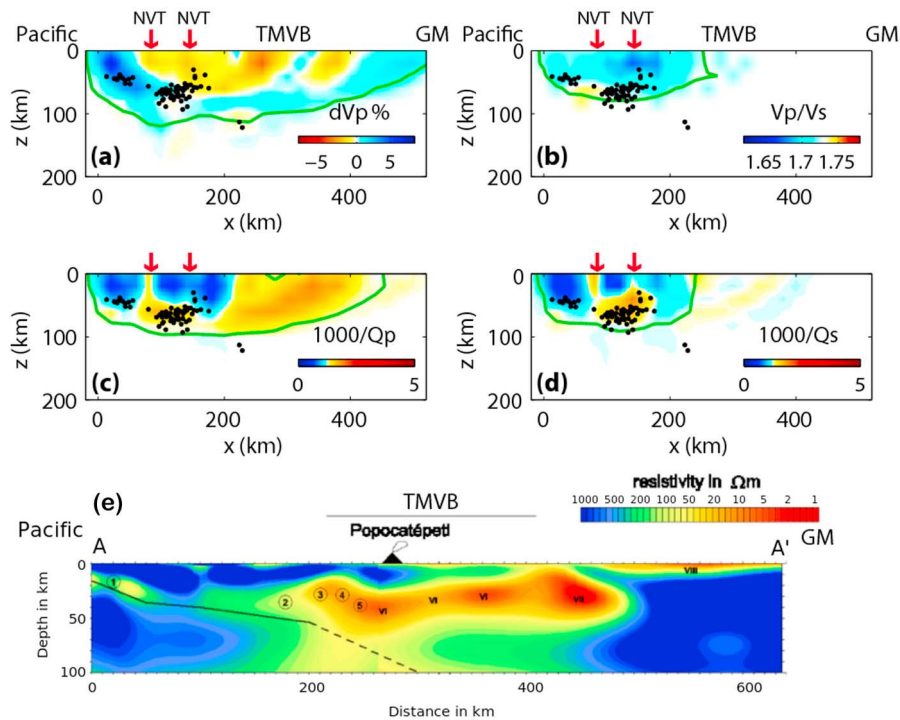


Figure 14. (a) P-wave velocity perturbation, (b) V_p/V_s , (c) P-wave attenuation, and (d) S-wave attenuation results for the slice $y = 0$ km, which is perpendicular to the trench, and crosses the TMVB. Black dots are earthquakes within 100 km from this slice. Red arrows denote the locations of two nonvolcanic tremor (NVT) clusters from *Payero et al.* [2008]. Green lines indicate the contour of the derivative weighted sum of 1000, and reasonably approximate the well-resolved region. (e) Resistivity results from a MT study along line AA' in Figure 1, which is almost the same line as $y = 0$ km (adapted from *Jödicke et al.* [2006]).

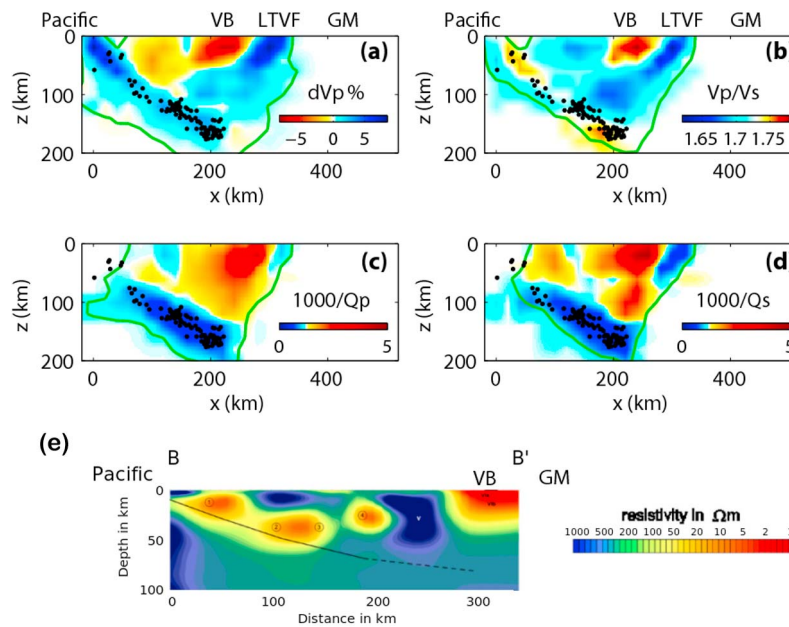


Figure 15. (a) P-wave velocity perturbation, (b) V_p/V_s , (c) P-wave attenuation, and (d) S-wave attenuation results for the slice $y = 450$ km, which is perpendicular to the trench and near the Tehuantepec Ridge. Black dots are earthquakes within 100 km from this slice. Green lines indicate the contour of the derivative weighted sum of 1000, and reasonably approximate the well-resolved region. (e) Resistivity results from a MT study along line BB' in Figure 1, which is close to the line as $y = 450$ km (adapted from Jödicke *et al.* [2006]).

on the inverted parameters, which may result in more extreme values. The high-attenuation/low-velocity region correlates with the low-resistivity zone from a MT study along a nearby line (Figure 14e) [Jödicke *et al.*, 2006]. High heat flow is also observed in the TMVB [Ziagos *et al.*, 1985]. The anomalies are probably caused by partial melts related to volcanism, or fluids released from the oceanic crust and sediments into the continental crust when the slab was underplating the continental crust beneath the TMVB during the flattening and rollback periods [Pérez-Campos *et al.*, 2008].

[26] The most prominent high-attenuation/low-velocity anomaly lies in the crust beneath the Veracruz Basin near the Isthmus of Tehuantepec (Figure 15). This anomaly also shows a high V_p/V_s ratio. Our study of the teleseismic velocity shows this anomaly too (Figure 12). Interestingly, MT studies along a line about 150 km to the west of the VEOX array (line BB' in Figure 1) show that low resistivity is also found beneath the Veracruz Basin west of the LTVF (Figure 15e) [Jödicke *et al.*, 2006]. The low-resistivity anomaly extends to the depth of about 40 km, which is about the same depth range where we see high attenuation, low- V_p and high V_p/V_s . Because of the possible smearing of the anomaly in the upper crust into the lower crust (Figure 11), this anomaly may be mainly related to the Veracruz Basin in the upper crust. If the anomaly indeed extends to the lower crust, the origin of it is not well understood, and may be related to some extinct volcanism in this complex tectonic region [Jödicke *et al.*, 2006].

[27] Beneath the active LTVF, we observe high velocity, low V_p/V_s and low attenuation (Figures 12 and 15). The high velocity beneath the LTVF has also been shown in a

previous teleseismic P-wave velocity study in Mexico [Gorbatov and Fukao, 2005], but at a much coarser resolution. The properties of this anomaly suggest that there is no large-scale partial melting zone associated with this volcanic field. Part of the high velocity and low attenuation may also be due to the relatively shallow Moho (~ 30 km) in this area [Kim *et al.*, 2010; Melgar and Pérez-Campos, 2011; Zamora-Camacho *et al.*, 2010]. The high velocity in the crust near the Pacific coast ($y = 0$ km, $y = 150$ km, $y = 300$ km and $y = 450$ km) and the crust near the Gulf of Mexico coast ($y = 300$ km and $y = 750$ km) may be due to the fact that the Moho in that area is shallower than the reference Moho depth [Castro, 2009]. The high velocity in the crust near the Pacific coast may also be partly due to the smearing of the high-velocity Cocos slab into the crust.

[28] Based on synthetic tests, the imaged dipping high-velocity structure from the teleseismic study may have a somewhat steeper angle than the real structure, especially for smaller dip angles (Figure 13 and Appendix A). Along the VEOX line, the seismicity and the opposite-dip anomaly from the receiver function studies both have relatively small dip angles of about 30° and 35° , respectively. Using an empirical correlation, the high-velocity structure dipping from the Pacific actually aligns with the relocated events, indicating the origin of the anomaly is the Cocos slab. With the correction, the high-velocity structure dipping from the Gulf of Mexico also has a dip angle similar to the discontinuity shown by the receiver function study [Kim *et al.*, 2011]. Kim *et al.* [2011] proposed that the unexpected slab from the Gulf of Mexico is caused by subduction of oceanic lithosphere before the collision between the Yucatán Block and Mexico in the Miocene. Our study shows that the Cocos

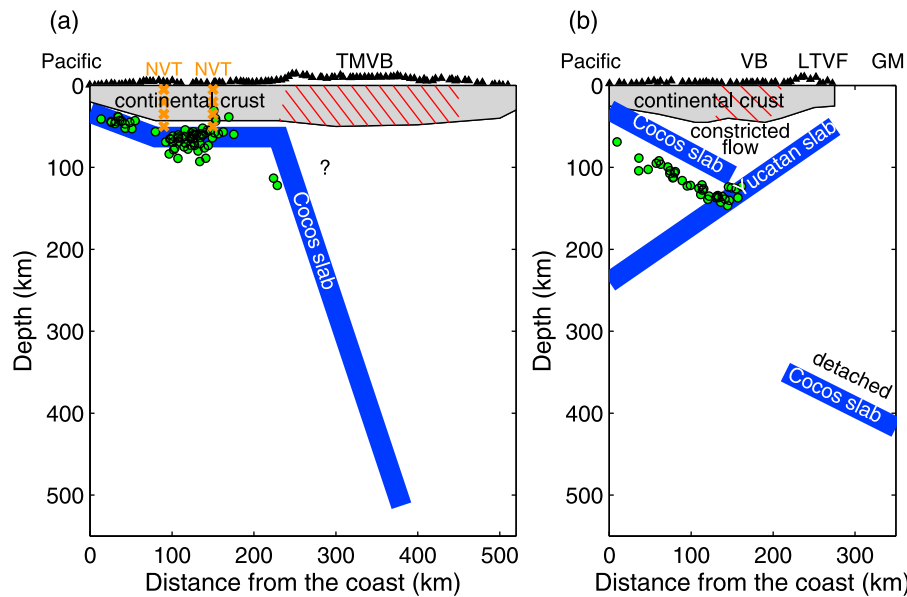


Figure 16. Interpretative section along (a) the MASE line and (b) the VEOX line. Green dots are earthquakes located near the line. The hatched areas indicate low velocity, high attenuation and low resistivity. The crosses represent the location of nonvolcanic tremors (NVT). Geographic labels are defined in Figures 1 and 12.

slab is truncated by the Yucatán slab at the depth of about 150 km. The break-off of the Cocos slab further to the south has also been proposed by *Rogers et al.* [2002]. In the teleseismic P-wave tomographic image of *Rogers et al.* [2002], the remnant of the Cocos slab is seen at the depth of below 350 km in the Gulf of Mexico, resulting a slab gap about 200 km wide (Figure 16). The unusual slab geometry near the Isthmus of Tehuantepec is likely to have a major effect on the dynamics of subduction in this region, and may shed light on the origin of the complex tectonic features [*Kim et al.*, 2011].

[29] Near the Isthmus of Tehuantepec, the mantle wedge shows moderate attenuation, relatively high V_p and low V_p/V_s (Figure 15), indicating a lack of partial melt. This suggests that the flow in the mantle wedge is constricted due to the geometry of the opposing Yucatán slab, and can explain the absence of a volcanic arc about 100 km above the Cocos slab. Low V_p/V_s have also been observed in the flat subduction wedge of the Andes [*Wagner et al.*, 2005]. At shallower depth above the Cocos slab, we observe relatively high attenuation, low V_p and moderate V_p/V_s . This may be related to the release of volatiles from the oceanic sediment and crust or only partially serpentinized forearc mantle. Low V_p and moderate V_p/V_s in the forearc mantle were also observed in the shallow Hikurangi subduction zone in New Zealand [*Eberhart-Phillips and Chadwick*, 2002].

[30] In the Guerrero segment, two clusters of nonvolcanic tremor (NVT) are observed above the flat slab [*Payero et al.*, 2008]. The depths of NVT are distributed between 5 and 40 km. The high attenuation we image above the flat slab shows some correlation with the location of NVT, especially for the S-wave attenuation (Figure 14). The V_p/V_s ratio, on the other hand, does not apparently correlate with the location of NVT. Although some relatively high V_p/V_s is found near the plate interface, it is not as high as what is found in

Japan where NVT occurs ($V_p/V_s > 1.8$) [*Shelly et al.*, 2006; *Matsubara et al.*, 2009]. This may indicate that the NVT in Guerrero is related to fluid release, but not necessarily highly overpressured free water.

7. Summary

[31] We have obtained 3D velocity and attenuation structure in central and southern Mexico. The results image the low-attenuation and high-velocity Cocos slab with the dip angle increasing from being almost flat in the central Guerrero segment to about 30° in the southern Oaxaca segment. High-attenuation and low-velocity anomalies are found beneath the TMVB and Veracruz Basin. An unexpected high-velocity structure dipping into the mantle from the Gulf of Mexico near the Isthmus of Tehuantepec is imaged by the teleseismic study. We interpret this unexpected dipping structure as the Yucatán slab caused by the collision between the Yucatán Block and Mexico in the Miocene. The Cocos slab is truncated by the Yucatán slab at the depth of about 150 km, and this configuration likely changes the convective flow in the mantle wedge.

Appendix A: Synthetic Tests for Dipping Structures With Teleseismic Data

[32] To understand the difference between the recovered dip angle and the input dip angle of the velocity anomaly with teleseismic data in Figure 13, we have done some synthetic tests. For a given input model, we construct the synthetic data by ray tracing earthquakes through the input model to each station on the VEOX array. Two types of synthetic tests have been done. In the first one, we fix the dip angle of the velocity anomaly to be 45° , and invert for the model using different earthquakes. Three different sets of teleseismic earthquakes

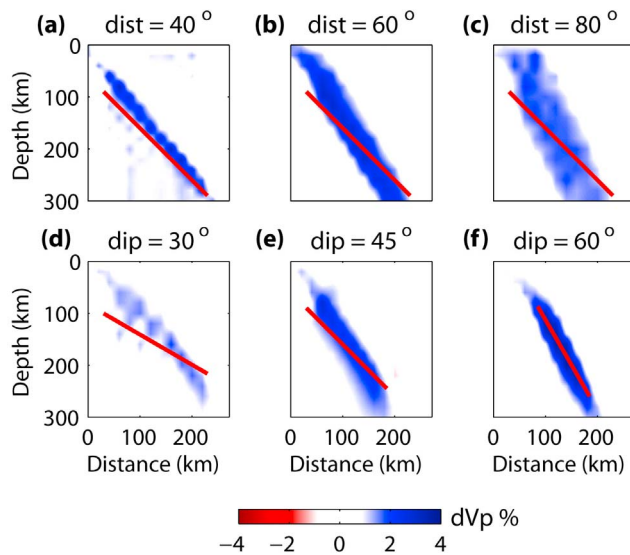


Figure A1. (a–c) Synthetic tests for a dipping structure of 45° using teleseismic earthquakes at different distances. (d–f) Synthetic tests for dipping structures of different degrees using teleseismic earthquakes with distances from 30° to 90° . Thickness of the anomaly is about 50 km and the position is indicated by the red line.

are used. Each set consists of earthquakes of the same distance (40° , 60° or 80°) but different azimuths (0° , 90° , 180° and 270°). In the second one, we vary the dip angle of the velocity anomaly from 30° to 60° , and invert for the model using the same set of earthquakes. The distances of earthquakes vary from 30° to 90° with an increment of 10° , and for each distance, different azimuths (0° , 90° , 180° and 270°) are covered.

[33] The synthetic tests show that for a given dipping structure, the inversion with earthquakes of shorter distance has smaller bias in the dip angle (Figures A1a–A1c). For the inversion with earthquakes covering distances between 30° and 90° , the bias in the dip angle is smaller for more steeply dipping structure (Figures A1d–A1f). The dip bias is introduced by the anisotropic shape of the point-spread function that is caused by the limited range of incidence angles.

[34] **Acknowledgments.** This study was supported by the Gordon and Betty Moore Foundation through the Tectonics Observatory at Caltech and NSF grant EAR0609707. Contribution 91 from the Caltech Tectonics Observatory. We would like to acknowledge Victor Hugo Espindola Castro for providing the SSN catalog. We thank Donna Eberhart-Phillips and Egill Hauksson for the help with the simul2000 package. We also thank Brandon Schmandt and Andreas Rietbrock for helpful discussions. Finally, we thank Editor Robert Nowack and two anonymous reviewers for helpful comments which improved the manuscript.

References

Alberto, C. A. O. (2010). Caracterización de la geometría de la zona benioff con una red densa de banda ancha en el istmo de Tehuantepec, PhD thesis, Natl. Auton. Univ. of Mex., Mexico City.

Anderson, J. G., and S. E. Hough (1984). A model for the shape of the Fourier amplitude spectrum of acceleration at high frequencies, *Bull. Seismol. Soc. Am.*, *74*(5), 1969–1993.

Brune, J. N. (1970). Tectonic stress and the spectra of seismic shear waves from earthquakes, *J. Geophys. Res.*, *75*(26), 4997–5009.

Campillo, M., S. K. Singh, N. Shapiro, J. Pacheco, and R. B. Herrmann (1996). Crustal structure south of the Mexican volcanic belt, based on group velocity dispersion, *Geophys. Int. Mex.*, *35*, 361–370.

Castro, R. R., J. G. Anderson, and S. K. Singh (1990). Site response, attenuation and source spectra of S waves along the Guerrero, Mexico, subduction zone, *Bull. Seismol. Soc. Am.*, *80*(6A), 1481–1503.

Castro, V. H. E. (2009). Modelos de velocidad cortical en Mexico, utilizando funciones de receptor en las estaciones de la red nacional de banda ancha, PhD thesis, Natl. Auton. Univ. of Mex., Mexico City.

Chen, T., and R. W. Clayton (2009). Seismic attenuation structure in central Mexico: Image of a focused high-attenuation zone in the mantle wedge, *J. Geophys. Res.*, *114*, B07304, doi:10.1029/2008JB005964.

Eberhart-Phillips, D. (1986). Three-dimensional velocity structure in northern California Coast Ranges from inversion of local earthquake arrival times, *Bull. Seismol. Soc. Am.*, *76*(4), 1025–1052.

Eberhart-Phillips, D. (1993). Local earthquake tomography: Earthquake source regions, in *Seismic Tomography: Theory and Practice*, edited by H. M. Iyer and K. Hirahara, pp. 613–643, CRC Press, Boca Raton, Fla.

Eberhart-Phillips, D., and M. Chadwick (2002). Three-dimensional attenuation model of the shallow Hikurangi subduction zone in the Raukumara Peninsula, New Zealand, *J. Geophys. Res.*, *107*(B2), 2033, doi:10.1029/2000JB000046.

Eberhart-Phillips, D., M. Reyners, M. Chadwick, and G. Stuart (2008). Three-dimensional attenuation structure of the Hikurangi subduction zone in the central North Island, New Zealand, *Geophys. J. Int.*, *174*, 418–434, doi:10.1111/j.1365-246X.2008.03816.x.

Ferrari, L., T. Tagami, M. Eguchi, M. Orozco-Esquivel, C. Petrone, J. Jacobo-Albarran, and M. López-Martínez (2005). Geology, geochronology and tectonic setting of late cenozoic volcanism along the southwestern Gulf of Mexico: The Eastern Alkaline Province revisited, *J. Volcanol. Geotherm. Res.*, *146*(4), 284–306.

García, D., S. K. Singh, M. Herraiz, J. F. Pacheco, and M. Ordaz (2004). Inslab earthquakes of central Mexico: Q, source spectra, and stress drop, *Bull. Seismol. Soc. Am.*, *94*(3), 789–802.

Gomberg, J. S., and T. G. Masters (1988). Waveform modelling using locked-mode synthetic and differential seismograms: Application to determination of the structure of Mexico, *Geophys. J. Int.*, *94*, 193–218, doi:10.1111/j.1365-246X.1988.tb05896.x.

Gomberg, J. S., K. F. Priestley, T. G. Masters, and J. N. Brune (1988). The structure of the crust and upper mantle of northern Mexico, *Geophys. J. Int.*, *94*(1), 1–20.

Gorbatov, A., and Y. Fukao (2005). Tomographic search for missing link between the ancient Farallon subduction and the present Cocos subduction, *Geophys. J. Int.*, *160*, 849–854, doi:10.1111/j.1365-246X.2005.02507.x.

Hauksson, E. (2000). Crustal structure and seismicity distribution adjacent to the Pacific and North America plate boundary in southern California, *J. Geophys. Res.*, *105*(B6), 13,875–13,904.

Husker, A., and P. M. Davis (2009). Tomography and thermal state of the Cocos plate subduction beneath Mexico City, *J. Geophys. Res.*, *114*, B04306, doi:10.1029/2008JB006039.

Iglesias, A., R. W. Clayton, X. Pérez-Campos, S. K. Singh, J. F. Pacheco, D. García, and C. Valdés-González (2010). S wave velocity structure below central Mexico using high-resolution surface wave tomography, *J. Geophys. Res.*, *115*, B06307, doi:10.1029/2009JB006332.

Jödicke, H., A. Jording, L. Ferrari, J. Arzate, K. Mezger, and L. Rüpke (2006). Fluid release from the subducted Cocos plate and partial melting of the crust deduced from magnetotelluric studies in southern Mexico: Implications for the generation of volcanism and subduction dynamics, *J. Geophys. Res.*, *111*, B08102, doi:10.1029/2005JB003739.

Kennett, B. L. N., and E. R. Engdahl (1991). Traveltimes for global earthquake location and phase identification, *Geophys. J. Int.*, *105*, 429–465, doi:10.1111/j.1365-246X.1991.tb06724.x.

Kim, Y., R. W. Clayton, and J. M. Jackson (2010). Geometry and seismic properties of the subducting Cocos plate in central Mexico, *J. Geophys. Res.*, *115*, B06310, doi:10.1029/2009JB006942.

Kim, Y. H., R. W. Clayton, and F. Keppie (2011). Evidence of a collision between the Yucatán Block and Mexico in the Miocene, *Geophys. J. Int.*, *187*, 989–1000.

Matsubara, M., K. Obara, and K. Kasahara (2009). High-Vp/Vs zone accompanying non-volcanic tremors and slow-slip events beneath southwestern Japan, *Tectonophysics*, *472*(1–4), 6–17.

Melgar, D., and X. Pérez-Campos (2011). Imaging the Moho and subducted oceanic crust at the Isthmus of Tehuantepec, Mexico, from receiver functions, *Pure Appl. Geophys.*, *168*, 1449–1460.

Meyer, R. P., J. S. Steinhart, and G. P. Woollard (1961). Central plateau, Mexico, in *Explosion Studies of Continental Structure*, edited by J. S. Steinhart and R. P. Meyer, pp. 199–225, Carnegie Inst. of Wash., Washington, D. C.

- Nelson, S. A., E. Gonzalez-Caver, and T. K. Kyser (1995), Constraints on the origin of alkaline and calc-alkaline magmas from the Tuxtla Volcanic Field, Veracruz, Mexico, *Contrib. Mineral. Petrol.*, *122*(1), 191–211.
- Ordaz, M., and S. K. Singh (1992), Source spectra and spectral attenuation of seismic waves from Mexican earthquakes, and evidence of amplification in the hill zone of Mexico City, *Bull. Seismol. Soc. Am.*, *82*(1), 24–43.
- Ottmüller, L., N. M. Shapiro, S. Krishna Singh, and J. F. Pacheco (2002), Lateral variation of Lg wave propagation in southern Mexico, *J. Geophys. Res.*, *107*(B1), 2008, doi:10.1029/2001JB000206.
- Pardo, M., and G. Suárez (1995), Shape of the subducted Rivera and Cocos plates in southern Mexico: Seismic and tectonic implications, *J. Geophys. Res.*, *100*(B7), 12,357–12,373, doi:10.1029/95JB00919.
- Payero, J. S., V. Kostoglodov, N. Shapiro, T. Mikumo, A. Iglesias, X. Pérez-Campos, and R. W. Clayton (2008), Nonvolcanic tremor observed in the Mexican subduction zone, *Geophys. Res. Lett.*, *35*, L07305, doi:10.1029/2007GL032877.
- Pérez-Campos, X., et al. (2008), Horizontal subduction and truncation of the Cocos Plate beneath central Mexico, *Geophys. Res. Lett.*, *35*, L18303, doi:10.1029/2008GL035127.
- Rietbrock, A. (2001), P wave attenuation structure in the fault area of the 1995 Kobe earthquake, *J. Geophys. Res.*, *106*(B3), 4141–4154.
- Rogers, R. D., H. Káráson, and R. D. van der Hilst (2002), Epeirogenic uplift above a detached slab in northern Central America, *Geology*, *30*(11), 1031–1034.
- Rychert, C. A., K. M. Fischer, G. A. Abers, T. Plank, E. Syracuse, J. M. Protti, V. Gonzalez, and W. Strauch (2008), Strong along-arc variations in attenuation in the mantle wedge beneath Costa Rica and Nicaragua, *Geochem. Geophys. Geosyst.*, *9*, Q10S10, doi:10.1029/2008GC002040.
- Schurr, B., G. Asch, A. Rietbrock, R. Trumbull, and C. Haberland (2003), Complex patterns of fluid and melt transport in the central Andean subduction zone revealed by attenuation tomography, *Earth Planet. Sci. Lett.*, *215*, 105–119, doi:10.1016/S0012-821X(03)00441-2.
- Schurr, B., A. Rietbrock, G. Asch, R. Kind, and O. Oncken (2006), Evidence for lithospheric detachment in the central Andes from local earthquake tomography, *Tectonophysics*, *415*(1–4), 203–223.
- Shapiro, N. M., M. Campillo, A. Paul, S. K. Singh, D. Jongmans, and F. J. Sánchez-Sesma (1997), Surface-wave propagation across the Mexican Volcanic Belt and the origin of the long-period seismic-wave amplification in the Valley of Mexico, *Geophys. J. Int.*, *128*, 151–166, doi:10.1111/j.1365-246X.1997.tb04076.x.
- Shelly, D. R., G. C. Beroza, S. Ide, and S. Nakamura (2006), Low-frequency earthquakes in Shikoku, Japan, and their relationship to episodic tremor and slip, *Nature*, *442*(7099), 188–191.
- Singh, S. K., J. F. Pacheco, D. Garcia, and A. Iglesias (2006), An estimate of shear-wave Q of the mantle wedge in Mexico, *Bull. Seismol. Soc. Am.*, *96*(1), 176–187.
- Singh, S. K., A. Iglesias, D. Garcia, J. F. Pacheco, and M. Ordaz (2007), Q of Lg waves in the central Mexican Volcanic Belt, *Bull. Seismol. Soc. Am.*, *97*(4), 1259–1266.
- Skinner, S. M., and R. W. Clayton (2011), An evaluation of proposed mechanisms of slab flattening in central Mexico, *Pure Appl. Geophys.*, *168*(8–9), 1461–1474.
- Stachnik, J. C., G. A. Abers, and D. H. Christensen (2004), Seismic attenuation and mantle wedge temperatures in the Alaska subduction zone, *J. Geophys. Res.*, *109*, B10304, doi:10.1029/2004JB003018.
- Thurber, C. H. (1993), Local earthquake tomography: Velocities and Vp/Vs theory, in *Seismic Tomography: Theory and Practice*, edited by H. M. Iyer and K. Hirahara, pp. 563–583, CRC Press, Boca Raton, Fla.
- Thurber, C., and D. Eberhart-Phillips (1999), Local earthquake tomography with flexible gridding, *Comput. Geosci.*, *25*(7), 809–818.
- Tsumura, N., S. Matsumoto, S. Horiuchi, and A. Hasegawa (2000), Three-dimensional attenuation structure beneath the northeastern Japan arc estimated from spectra of small earthquakes, *Tectonophysics*, *319*, 241–260, doi:10.1016/S0040-1951(99)00297-8.
- Um, J., and C. Thurber (1987), A fast algorithm for two-point seismic ray tracing, *Bull. Seismol. Soc. Am.*, *77*(3), 972–986.
- Valdes, C. M., W. D. Mooney, S. K. Singh, R. P. Meyer, C. Lomnitz, J. H. Luetgert, C. E. Helsley, B. T. R. Lewis, and M. Mena (1986), Crustal structure of Oaxaca, Mexico, from seismic refraction measurements, *Bull. Seismol. Soc. Am.*, *76*(2), 547–563.
- Verma, S. P. (2006), Extension-related origin of magmas from a garnet-bearing source in the Los Tuxtlas volcanic field, Mexico, *Int. J. Earth Sci.*, *95*(5), 871–901.
- Wada, I., and K. Wang (2009), Common depth of slab-mantle decoupling: Reconciling diversity and uniformity of subduction zones, *Geochem. Geophys. Geosyst.*, *10*, Q10009, doi:10.1029/2009GC002570.
- Wagner, L. S., S. Beck, and G. Zandt (2005), Upper mantle structure in the south central Chilean subduction zone (30° to 36°S), *J. Geophys. Res.*, *110*, B01308, doi:10.1029/2004JB003238.
- Yamamoto, J., L. Quintanar, R. B. Herrmann, and C. Fuentes (1997), Lateral variations of Lg coda Q in southern Mexico, *Pure Appl. Geophys.*, *149*(3), 575–599.
- Zamora-Camacho, A., V. H. Espindola, J. F. Pacheco, J. M. Espindola, and M. L. Godinez (2010), Crustal thickness at the Tuxtla volcanic field (Veracruz, Mexico) from receiver functions, *Phys. Earth Planet. Inter.*, *182*, 1–9, doi:10.1016/j.pepi.2010.05.009.
- Ziagos, J. P., D. D. Blackwell, and F. Mooser (1985), Heat flow in southern Mexico and the thermal effects of subduction, *J. Geophys. Res.*, *90*(B7), 5410–5420.